Precision Engineering 96 (2025) 160–169

Contents lists available at ScienceDirect

Precision Engineering

journal homepage: www.elsevier.com/locate/precision

Design, modeling and control of a 3 degree-of-freedom positioning system for high-precision 3D inline-metrology

Daniel Pechgraber [a,b,*], Ernst Csencsics [a,b], Georg Schitter [a]

[a] Automation and Control Institute TU Wien, Vienna, 1040, Austria
[b] Christian Doppler Laboratory for Precision Measurements in Motion, Automation and Control Institute TU Wien, Vienna, 1040, Austria

ARTICLE INFO

Keywords:
Precision positioning system
Dual-stage actuation
Decoupled motion control
Inline metrology

ABSTRACT

This paper presents the mechatronic design and control of a 3 degree-of-freedom (3-DoF) precision positioning system for high-precise optical 3D inline-metrology based on a dual-stage approach. It overcomes limitations of common optical 3D measurement systems due to motion blur by precisely positioning measurement systems on a metrology platform with respect to a (moving) measurement sample and additionally extends their measurement range. A comprehensive mathematical model of the system is derived and simplified to linear models suitable for classical linear control design methods. Using a modal analysis approach for system decoupling, a decentralized control scheme with individual Single-Input Single-Output controllers is developed for precisely controlling the metrology platform position in 3 DoFs. Experimental measurements on the prototype system demonstrate a maximum measurement error resulting from the positioning system of down to 7.5 µm to 12.3 µm (rms) during platform motion of up to 100 mm/s over a large inspection area (0.7 m × 0.5 m), as well as 147 nm (rms) error during static positioning.

1. Introduction

Inline measurement systems are essential in today's industrial manufacturing and production environments, as they enable high precision, throughput and continuous quality control [1,2]. Optical 3D measurement systems, such as laser line and structured light sensors, are frequently employed in a multitude of industrial applications for this purpose [3,4]. However, as production systems advance, these optical measurement systems increasingly face challenges in meeting the required speed and precision demands, with motion blur posing a significant constraint on the achievable measurement precision [5]. Furthermore, external disturbances like vibrations from the production environment pose a significant challenge for measurement systems working directly in-line [6].

To address these challenges, vibration-insensitive measurement techniques have been developed, which however cannot fully mitigate larger disturbance magnitudes [7]. A promising solution involves the precise motion control of the optical measurement system with respect to the measurement sample, i.e. actively tracking the sample, allowing for highly accurate 3D surface measurements on moving objects [8]. By maintaining zero relative motion between sample and measurement system, local lab-like conditions can be created. Additionally, the measurement range can be arbitrarily extended within the capabilities of the positioning system, which is beneficial, when e.g. moving laser-line sensors across samples to obtain 3D surface measurements [9]. Nevertheless, the measurement precision in the moving direction depends heavily on the positioning system, especially considering parasitic rotations of the measurement system with respect to the motion plane of the sample.

A common approach for precise positioning over long ranges is dual-stage actuation, which combines two actuation principles [10]. Usually a less precise coarse actuator is used for positioning over a long range, while a more precise actuator with a small actuation range is mounted in series. This approach can be found in a large number of applications, ranging from hard-disk drives to wafer scanners [11,12]. For the fine actuators often electro-magnetic Lorentz-actuators (LAs) are used, due to their favorable properties, such as the linear force to current relation and (quasi) zero-stiffness [13,14]. Zero-stiffness refers to a position independent actuator force, which inherently isolates the mover from disturbing vibrations. This makes them well suited for precision positioning based on the dual-stage approach, since disturbance forces from the coarse actuator are not transmitted to the fine actuator [15]. The moving part is usually constrained in the non-actuated degrees of freedom (DoFs) by either magnetic levitation or air-bearings [8,16] to maintain the zero stiffness property, or by mechanical flexures in combination with a high-bandwidth position control loop [15].

* Correspondence to: Automation and Control Institute, TU Wien, Gußhausstraße 27-29, Vienna, 1040, Austria.
E-mail address: pechgraber@acin.tuwien.ac.at (D. Pechgraber).

https://doi.org/10.1016/j.precisioneng.2025.05.015
Received 20 November 2024; Received in revised form 8 April 2025; Accepted 19 May 2025
Available online 5 June 2025

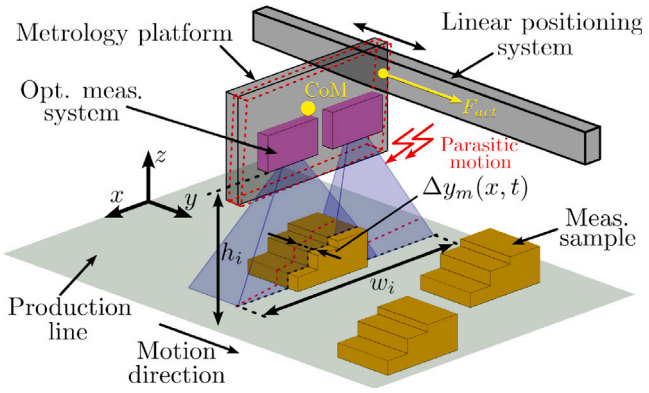

Fig. 1. Principle of a 3D inline-measurement system with moving optical measurement systems, tracking measurement samples on the production line. Parasitic motion of the metrology platform leads to a lateral measurement error $\Delta y_m(x,t)$ on the sample.

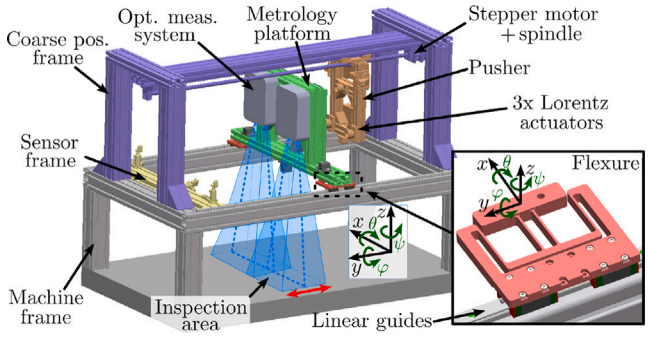

Fig. 2. General system design: The metrology platform, which holds the optical measurement systems, is guided with flexure mounts on linear roller guides. The pusher connected to the mechanical spindle-drive controls the platform position in 3DoFs.

The contribution of this paper is the mechatronic design as well as the mathematical modeling and decoupled control of a 3-DoF precision positioning system for 3D inline-metrology applications. The novel linear positioning system is based on a dual-stage approach, integrating multiple fine actuators on top of a single long-range coarse actuator.

2. System design

At first the requirements and challenges for the target application are outlined, as basis for the subsequent system design.

2.1. System requirements and challenges

In Fig. 1 a principle sketch of a 3D inline-measurement system is shown, which incorporates a movable metrology platform, carrying optical measurement systems. For precise inline-measurement, it is necessary to achieve high-precision motion in one translational direction (y) over a long range, while maintaining a constant and stable orientation of the metrology platform with respect to the measurement sample [8]. Key challenges arise from unbalanced inertia, where the actuation force of the linear positioning system F_{act} is not aligned with the center of mass (CoM) of the platform, leading to parasitic rotations and measurement errors $\Delta y_m(x,t)$ of the sample. Additionally, reaction forces from the measurement systems (e.g. scanning systems) and external disturbances can induce unwanted parasitic motion, degrading measurement accuracy. These factors are critical in high-precision inline-metrology applications, where measurement accuracies on the scale of single microns are desired. The system must therefore actively control multiple DoFs with high precision to mitigate these adverse effects. To further provide a large inspection area, linear motion ranges up to meters are desired. Another key requirement is cost-effectiveness, to be also competitive in industrial applications with steadily growing precision demands, such that low-cost components are preferred in the mechatronic system design.

2.2. System design and integration

Based on the system requirements and challenges, a positioning system is designed which is shown in Fig. 2, integrated into an inline-metrology system.

Core part of the system is the metrology platform incorporating the optical measurement systems, which is moved along the y-direction of the inspection area (production line). A standard spindle-drive with a stepper motor is used for the coarse positioning, reducing system complexity and costs and providing extendable travel ranges. To overcome the low positioning precision of mechanical spindle-drives, a dual-stage approach is applied. Therefore the coils of three cylindrical LAs are mounted on the pusher, which is connected to the spindle-drive. The magnet parts of the LAs are fixed at the metrology platform, allowing the positioning of the platform in 3 DoFs by applying forces from the back. It is suspended on the machine frame by linear roller guides on either side of the frame. For this reason, disturbing vibrations or parasitic motion from the spindle-drive are isolated from the metrology platform due to the zero-stiffness property of the LAs.

To counteract manufacturing and mounting tolerances of the linear guides, mechanical flexure mounts are designed to enable sufficient motion freedom, which allows the LAs to position the metrology platform in constant orientation to the inspection area over the entire motion range. The mounts are designed as double parallelogram flexure structure (red in Fig. 2), which is also referred to as crab-leg flexure [17]. This structure allows a relatively low stiffness in the actuated translational direction y and the rotations θ and ψ, while providing a high stiffness in the other directions (x, z and φ), restricting movement in the non-actuated DoFs.

To accurately position the platform with respect to the measurement sample, a separate sensor frame is connected to the machine frame, which is considered to have negligible parasitic motion relative to the inspection area. Position measurement in the 3 actuated DoFs (y, θ, ψ) is done via 3 optical position sensors mounted on the sensor frame. Additionally, an optical proximity sensor is mounted on the pusher to determine the relative position between the coarse positioning unit and the platform.

3. Mathematical system model

In this section a detailed mathematical system model of the designed system is presented, which serves as the basis for the decoupling of the DoFs and the control design in the next sections. It is important to note that, in principle, a generic system model could be derived based on the system identification presented in Section 4. However, an analytical parametric model provides deeper physical insight into how each system parameter influences the system dynamics, which is particularly valuable when scaling the system or adapting it for applications with different geometries or DoFs.

3.1. Equations of motion

The dynamic system model describing the motion of the dual-stage actuated metrology platform is derived based on the Euler–Lagrange equations [18]

$$\frac{\mathrm{d}}{\mathrm{d}t}\frac{\partial T}{\partial \dot{q}_j} - \frac{\partial T}{\partial q_j} + \frac{\partial U}{\partial q_j} = f_{q,j}, \quad j = 1, \ldots, n, \tag{1}$$

for the generalized coordinates q_j, the kinetic energy T, the velocity-independent potential U, and the corresponding generalized forces $f_{q,j}$.

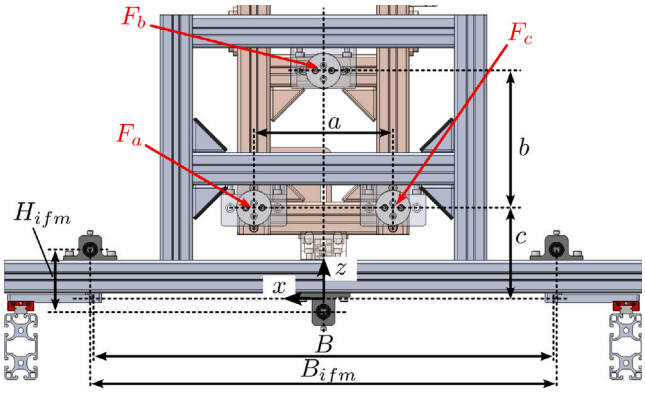

Fig. 3. Dimensions of the metrology platform (Front view).

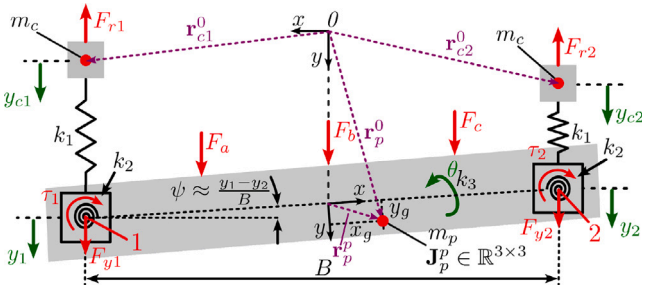

Fig. 4. Sketch of the mechanical system model (top view). The flexure mounts on either side are modeled by 3 stiffness coefficients k_1, k_2 and k_3. The metrology platform is modeled as rigid body with the mass m_p, the coordinates of the center of mass (x_g, y_g, z_g) and inertia matrix $\mathbf{J}^b_s$ defined in the body-fixed coordinate frame. The generalized coordinates $\mathbf{q}$ are highlighted in green. (For interpretation of the references to color in this figure legend, the reader is referred to the web version of this article.)

In Fig. 3, the front view of the platform (without meas. systems) is shown with the dimensions relevant for the model derivation. Additionally, a sketch of the mechanical model is depicted in Fig. 4. It is assumed, that the platform acts as a rigid body with constant and diagonal inertia matrix $\mathbf{J}^p_p = \text{diag}\left(J_{xx}, J_{yy}, J_{zz}\right) \in \mathbb{R}^{3\times3}$ defined in the center of mass in the body-fixed coordinate frame. The platform is connected to the linear carts of the machine frame (lumped masses m_c) by the flexure mounts on either side. Since the aim of the control will be to hold the metrology platform in a constant orientation with respect to the production line (Fig. 2), only small deformations of the flexure mounts are assumed. Therefore they are modeled as 3 independent linear springs with translational spring constant k_1 and two rotational spring constants k_2 and k_3 with their respective viscous damping coefficients (d_1, d_2, d_3) [19]. The fine-positioning of the platform is done by controlling the forces in the three LAs at the back of the platform. These forces (F_a, F_b, F_c) together with (non-linear) friction forces acting on the linear carts (F_{r1}, F_{r2}) are the inputs for the dynamic system model and are combined in the force vector $\mathbf{f}^e = \begin{bmatrix} F_a & F_b & F_c & F_{r1} & F_{r2} \end{bmatrix}^{\mathrm{T}}$. For the mechanical model in Fig. 4 5 generalized coordinates

$$\mathbf{q} = \begin{bmatrix} y_1 & y_{c1} & y_2 & y_{c2} & \theta \end{bmatrix}^{\mathrm{T}} \tag{2}$$

are defined with y_1 and y_2 being the translational position of the horizontal crossbar on either side, y_{c1} and y_{c2} being the translational position of the linear carts and θ being the rotation around the x-axis of the body-fixed coordinate frame.

In order to derive the kinetic energy T, the potential U and the generalized forces $f_{q,j}$ for each degree of freedom, kinematic transformations from the body-fixed coordinate frames into the world coordinate frame depending on the generalized coordinates $\mathbf{q}$ are required. Therefore the transformation

$$\mathbf{H}^i_0 = \begin{bmatrix} \mathbf{R}^i_0 & \mathbf{d}^i_0 \\ \mathbf{0} & 1 \end{bmatrix} \tag{3}$$

with the translational displacement $\mathbf{d}^i_0$ and the rotation $\mathbf{R}^i_0$ between the body-fixed i-coordinate frame and the world coordinate frame (0) is introduced, which is used to express rigid body positions in the world coordinate frame

$$\mathbf{P}_0 = \mathbf{H}^i_0 \mathbf{P}_i\,, \quad \text{with} \quad \mathbf{P}_i = \begin{bmatrix} \mathbf{p}_i \\ 1 \end{bmatrix}. \tag{4}$$

For the metrology platform the transformation is obtained by

$$\mathbf{R}^p_0 = \begin{bmatrix} \cos\left(\frac{y_1-y_2}{B}\right) & -\sin\left(\frac{y_1-y_2}{B}\right) & 0 \\ \cos(\theta)\sin\left(\frac{y_1-y_2}{B}\right) & \cos(\theta)\cos\left(\frac{y_1-y_2}{B}\right) & -\sin(\theta) \\ \sin(\theta)\sin\left(\frac{y_1-y_2}{B}\right) & \sin(\theta)\cos\left(\frac{y_1-y_2}{B}\right) & \cos(\theta) \\ 0 & 0 & 0 \end{bmatrix},$$
$$\mathbf{d}^p_0 = \begin{bmatrix} 0 \\ \frac{y_1}{2} + \frac{y_2}{2} \\ 0 \end{bmatrix}, \tag{5}$$

considering standard rotations around the body-fixed z-axis with the angle $\tan^{-1}\left(\frac{y_1-y_2}{B}\right) \approx \frac{y_1-y_2}{B}$ and the x-axis with θ. The other transformations include only translations and are given by

$$\mathbf{R}^{c1}_0 = \mathbf{R}^{c2}_0 = \mathbf{I},\ \mathbf{d}^{c1}_0 = \begin{bmatrix} \frac{B}{2} \\ y_{c1} \\ 0 \end{bmatrix}, \text{ and } \mathbf{d}^{c2}_0 = \begin{bmatrix} -\frac{B}{2} \\ y_{c2} \\ 0 \end{bmatrix}. \tag{6}$$

Using the defined homogeneous transformations (4)–(6), the velocities of the centers of gravity can be expressed as function of the generalized coordinates by[1]

$$\dot{\mathbf{r}}^0_i = \frac{\mathrm{d}}{\mathrm{d}t}\left(\mathbf{H}^i_0 \mathbf{r}^i_i\right) = \dot{\mathbf{H}}^i_0 \mathbf{r}^i_i + \underbrace{\mathbf{H}^i_0 \dot{\mathbf{r}}^i_i}_{=0}. \tag{7}$$

Similarly, with the linear operator $\Gamma\{*\}$ applied to $* \in \mathbb{R}^{3\times3}$

$$\Gamma\{*\} = \text{diag}\left(\begin{bmatrix} 0 & 0 & 1 \\ 1 & 0 & 0 \\ 0 & 1 & 0 \end{bmatrix} * \begin{bmatrix} 0 & 0 & 1 \\ 1 & 0 & 0 \\ 0 & 1 & 0 \end{bmatrix}\right), \tag{8}$$

the rotation rates $\boldsymbol{\omega}^0_i$ of the rigid bodies can be derived with the rotation matrices $\mathbf{R}^i_0$ by [20]

$$\boldsymbol{\omega}^0_i = \Gamma\left\{\dot{\mathbf{R}}^i_0 \left(\mathbf{R}^i_0\right)^{\mathrm{T}}\right\}. \tag{9}$$

With these formulations the kinetic energy of the system can be expressed by

$$T = T_{trans} + T_{rot} \tag{10}$$

with

$$T_{trans} = \sum_i \frac{1}{2} m_i \left(\dot{\mathbf{r}}^0_i\right)^{\mathrm{T}} \dot{\mathbf{r}}^0_i \quad i \in \{p, c1, c2\},$$
$$T_{rot} = \frac{1}{2}\left(\boldsymbol{\omega}^0_i\right)^{\mathrm{T}} \mathbf{J}^0_p \boldsymbol{\omega}^0_i, \tag{11}$$

and the inertia matrix of the metrology platform in the world coordinate frame

$$\mathbf{J}^0_p = \mathbf{R}^p_0 \mathbf{J}^p_p \left(\mathbf{R}^p_0\right)^{\mathrm{T}}. \tag{12}$$

The potential U contains gravitational forces acting on the rigid bodies and spring forces related to the flexure mounts on either side.

[1] If vectors $\mathbf{r}$ are multiplied with $\mathbf{H}$, they are extended to $\begin{bmatrix} \mathbf{r}^T & 1 \end{bmatrix}^T$ and the resulting 4th vector entry is removed.

With the gravitational vector $\mathbf{g}^0 = \begin{bmatrix} 0 & 0 & -g \end{bmatrix}^{\mathrm{T}}$ it can be calculated by

$$\begin{aligned} U = &- m_p \left(\mathbf{g}^0\right)^{\mathrm{T}} \cdot \mathbf{r}_p^0 - m_c \left(\mathbf{g}^0\right)^{\mathrm{T}} \cdot \mathbf{r}_{c1}^0 - m_c \left(\mathbf{g}^0\right)^{\mathrm{T}} \cdot \mathbf{r}_{c2}^0 \\ &+ \frac{1}{2} k_1 \left(y_1 - y_{c1}\right)^2 + \frac{1}{2} k_1 \left(y_2 - y_{c2}\right)^2 \\ &+ k_2 \left(\frac{y_1 - y_2}{B}\right)^2 + k_3 \theta^2 , \end{aligned} \tag{13}$$

with the assumption $\tan^{-1}\left(\frac{y_1 - y_2}{B}\right) \approx \frac{y_1 - y_2}{B}$, which is justified by the small (ideally zero) rotations around the z-axis. It is to be noted, that the z-position of the linear-carts in the world coordinate frame is constant and the contribution of the linear carts vanishes in the partial derivative in the equations of motion (1).

The external forces $\mathbf{f}_q$ on the right side of (1) are comprised of external actuator as well as friction forces $\mathbf{f}_q^e$ and dissipative forces related to the damping of the flexure mounts $\mathbf{f}_q^d$ according to

$$\mathbf{f}_q = \mathbf{f}_q^e + \mathbf{f}_q^d . \tag{14}$$

To calculate the contribution from actuator and friction forces, the force attack points and directions have to be defined in the world coordinate frame. As the rotations around the body-fixed x-and z-axis are very small during system operation, it is assumed that the VCA-forces only have components in global y-direction of the world coordinate frame. The force vectors of the actuator and friction forces are therefore defined as

$$\mathbf{f}_j^0 = \begin{cases} \begin{bmatrix} 0 & F_j & 0 \end{bmatrix}^T , & j \in \{a, b, c\} \\ \begin{bmatrix} 0 & -F_j & 0 \end{bmatrix}^T , & j \in \{r1, r2\} . \end{cases} \tag{15}$$

The attack points of the forces are defined in the body-fixed frame

$$\begin{aligned} &\mathbf{r}_a^s = \begin{bmatrix} \frac{a}{2} & -d & c \end{bmatrix}^{\mathrm{T}}, \mathbf{r}_b^s = \begin{bmatrix} 0 & -d & b + c \end{bmatrix}^{\mathrm{T}} , \\ &\mathbf{r}_c^s = \begin{bmatrix} -\frac{a}{2} & -d & c \end{bmatrix}^{\mathrm{T}}, \mathbf{r}_{r1}^s = \begin{bmatrix} \frac{B}{2} & 0 & 0 \end{bmatrix}^{\mathrm{T}}, \mathbf{r}_{r2}^s = \begin{bmatrix} -\frac{B}{2} & 0 & 0 \end{bmatrix}^{\mathrm{T}} . \end{aligned} \tag{16}$$

The generalized force related to external forces is then calculated by

$$\mathbf{f}_q^e = \sum_j \underbrace{J_{\mathbf{q}}\left(\mathbf{H}_0^p \mathbf{r}_j^p\right)^{\mathrm{T}}}_{\mathbf{r}_j^0} \mathbf{f}_j^0 \quad j \in \{a, b, c, r1, r2\} , \tag{17}$$

with $J_{\mathbf{q}}(*)$ being the Jacobian matrix with respect to the generalized coordinates $\mathbf{q}$.

For the force related to damping, the rotation around the global z-axis is defined as $\psi = tan^{-1}\left(\frac{y_1 - y_2}{B}\right) \approx \frac{y_1 - y_2}{B}$, so the torque related to damping in the points 1 and 2 from Fig. 4 is given by

$$\tau_1 = \tau_2 = -d_2 \frac{\dot{y}_1 - \dot{y}_2}{B} . \tag{18}$$

Under the assumption of small rotation angles ψ and symmetrical considerations, the resulting damping force components in the points 1 and 2 are assumed to have only y-components in the global coordinate-frame given by

$$F_{y1} = -F_{y2} \approx \frac{\tau_1 + \tau_2}{B/2} = -4 d_2 \frac{\dot{y}_1 - \dot{y}_2}{B^2} . \tag{19}$$

The generalized force related to damping follows with

$$\mathbf{f}_q^d = \begin{bmatrix} -d_1 \left(\dot{y}_1 - \dot{y}_{c1}\right) - 4 d_2 \frac{\dot{y}_1 - \dot{y}_2}{B^2} \\ d1 \left(\dot{y}_1 - \dot{y}_{c1}\right) \\ -d_1 \left(\dot{y}_2 - \dot{y}_{c2}\right) + 4 d_2 \frac{\dot{y}_1 - \dot{y}_2}{B^2} \\ d_1 \left(\dot{y}_2 - \dot{y}_{c2}\right) \\ -d_3 \dot{\theta} \end{bmatrix} . \tag{20}$$

By substituting (10) and (13), together with their derivatives using the chain-rule of differentiation [20], and the generalized forces (14) into the Euler–Lagrange equations (1), a set of coupled second-order differential equations are obtained. The equations can be written in matrix form as

$$\mathbf{M}(\mathbf{q})\ddot{\mathbf{q}} + \mathbf{C}(\mathbf{q}, \dot{\mathbf{q}})\dot{\mathbf{q}} + \mathbf{N}(\mathbf{q}, \dot{\mathbf{q}}) = \mathbf{f}_q^e = \mathbf{W}(\mathbf{q})\mathbf{f}^e \tag{21}$$

in which the input forces of the model $\mathbf{f}^e$ are mapped to the generalized external forces $\mathbf{f}_q^e$ with the matrix $\mathbf{W}(\mathbf{q})$, which is calculated by solving (17) for each entry of $\mathbf{f}^e$. The generalized forces related to damping $\mathbf{f}_q^d$ are included in the matrix $\mathbf{N}$.

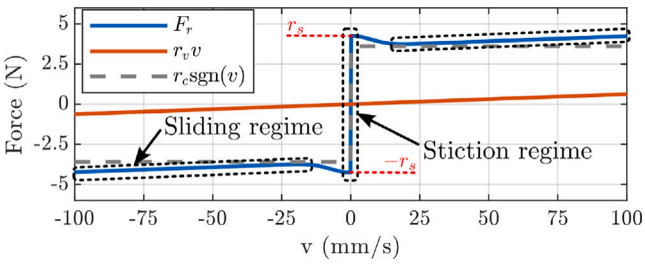

Fig. 5. Friction force on linear carts based on static Lu-Gre friction model.

3.2. Linear cart friction

The definition of the friction forces as part of the external input forces $\mathbf{f}^e$ in the general model (21) allows the formulation of a general friction model. There exist many different friction models in the literature that include different physical effects. A commonly used model is the dynamical Lu-Gre friction model, which can also describe stick/slip motion resulting from the Stribeck effect [21]. For reasons of simplicity, a static formulation of the Lu-Gre friction model [21]

$$F_r = r_c \mathrm{sgn}(v) + r_v v + (r_s - r_c) \exp\left\{ -\left(\frac{v}{v_0}\right)^2 \right\} \mathrm{sgn}(v) \tag{22}$$

with the linear-cart velocity v, the Coulomb friction r_c, viscous friction r_v, stiction force r_s and the reference velocity v_0 is used to describe the friction force acting on the linear carts. The friction force over linear-cart velocity is shown in Fig. 5. As the force curve is non-continuous at $v = 0$, two friction regimes can be defined. For an external linear cart force below the stiction force r_s, the cart motion is zero, referred to as stiction regime. Consequently, for an external force beyond r_s, the cart starts to move, which is referred to as sliding regime.

3.3. Reduced linear models

The general (non-linear) system model is good for approximating the real system behavior over the entire motion range, but it is not suited for linear control design. Therefore, this section will demonstrate that the system's behavior can be effectively approximated using simplified linear models within the intended operational range. First it is to mention, that two linear models are derived, one for each of the previously defined friction regimes.

In the stiction regime it is assumed, that the force acting on the linear-carts is smaller than the stiction force r_s. Consequently, the cart motion is negligible and the condition $y_{c1} = y_{c2} = \text{const.}$ is satisfied. Therefore the two generalized coordinates y_{c1} and y_{c2} and their respective equations of motion can be omitted in the system model (21). If further only very small and slow rotations of the platform around the body-fixed x- and z-axis are allowed, the terms $(y_1 - y_2)$, θ, $(\dot{y}_1 - \dot{y}_2)$ and $\dot{\theta}$ can be neglected in (21), considering that $y_1 - y_2 = 0$ and $\theta = 0$ are conditions for a constant orientation of the measurement systems and fixed by the later developed feedback control loop. Under these assumption the Coriolis matrix $\mathbf{C}(\mathbf{q}, \dot{\mathbf{q}})$ vanishes entirely, and (21) can be reduced to the coupled linear mechanical system

$$\mathbf{M}_r \ddot{\mathbf{q}}_r + \mathbf{D}\dot{\mathbf{q}}_r + \mathbf{K}\mathbf{q}_r = \mathbf{W}_r \mathbf{f}_r^e , \tag{23}$$

with the constant mass matrix $\mathbf{M}_r \in \mathbb{R}^{3\times3}$, damping matrix $D \in \mathbb{R}^{3\times3}$ and stiffness matrix $\mathbf{K} \in \mathbb{R}^{3\times3}$ with the reduced coordinates $\mathbf{q}_r = \begin{bmatrix} y_1 & y_2 & \theta \end{bmatrix}^T$, the reduced force vector $\mathbf{f}_r^e = \begin{bmatrix} F_a & F_b & F_c \end{bmatrix}^T$ and

$$\mathbf{W}_r = \begin{bmatrix} \frac{a+B}{2B} & \frac{1}{2} & \frac{-a+B}{2B} \\ \frac{-a+B}{2B} & \frac{1}{2} & \frac{a+B}{2B} \\ -c & -c-b & -c \end{bmatrix}. \tag{24}$$

In a similar manner the model for the sliding regime of the linear carts is derived under the assumption of no relative motion between the linear carts and the horizontal cross-bar of the metrology platform. This means that the conditions $y_1 = y_{c1}$ and $y_2 = y_{c2}$ are satisfied, which is justified if using a high stiffness k_1 and by the fact, that the platform carrying the measurement systems is much heavier than the linear carts ($m_p \gg m_c$). In this case, the linear carts are moving and therefore friction has to be considered. To keep the model linear, the viscous friction part r_v of (22) is considered, whereas the non-linear parts are neglected as the later designed position control system deals with it. Considering the same simplifications as in the stiction regime regarding the platform movement ($y_1 - y_2 = 0, \ldots$), a linear coupled mechanical model with the same structure and coordinates as (23) can be derived. The mass matrix $\mathbf{M}_r = \begin{bmatrix} \mathbf{m}_1 & \mathbf{m}_2 & \mathbf{m}_3 \end{bmatrix}$ is the same in both cases, but the stiffness and damping matrices change due to the made assumptions (e.g. stiffness k_1 vanishes for the sliding regime due to $y_1 = y_{c1}$ and $y_2 = y_{c2}$). The system matrices for both regimes are given by

$$\mathbf{m}_1 = \begin{bmatrix} \frac{m_p\left(B^2+4Bx_g+4x_g^2+4y_g^2\right)+4I_{zz}}{4B^2} \\ \frac{m_p\left(B^2-4x_g^2-4y_g^2\right)-4I_{zz}}{4B^2} \\ -\frac{m_p z_g\left(B+2x_g\right)}{2B} \end{bmatrix}, \mathbf{m}_2 = \begin{bmatrix} \frac{m_p\left(B^2-4x_g^2-4y_g^2\right)-4I_{zz}}{4B^2} \\ \frac{m_p\left(B^2-4Bx_g+4x_g^2+4y_g^2\right)+4I_{zz}}{4B^2} \\ -\frac{m_p z_g\left(B-2x_g\right)}{2B} \end{bmatrix},$$

$$\mathbf{m}_3 = \begin{bmatrix} -\frac{m_p z_g\left(B+2x_g\right)}{2B} \\ -\frac{m_p z_g\left(B-2x_g\right)}{2B} \\ m_p\left(y_g^2+z_g^2\right)+I_{xx} \end{bmatrix}, \mathbf{K}^{sl} = \begin{bmatrix} \frac{2k_2}{B^2} & -\frac{2k_2}{B^2} & \frac{m_p x_g g}{B} \\ -\frac{2k_2}{B^2} & \frac{2k_2}{B^2} & -\frac{m_p x_g g}{B} \\ \frac{m_p x_g g}{B} & -\frac{m_p x_g g}{B} & -g m_p z_g + 2k_3 \end{bmatrix},$$

$$\mathbf{D}^{st} = \begin{bmatrix} d_1+\frac{4d_2}{B^2} & -\frac{4d_2}{B^2} & 0 \\ -\frac{4d_2}{B^2} & d_1+\frac{4d_2}{B^2} & 0 \\ 0 & 0 & d_3 \end{bmatrix}, \quad \mathbf{D}^{sl} = \begin{bmatrix} r_v+\frac{4d_2}{B^2} & -\frac{4d_2}{B^2} & 0 \\ -\frac{4d_2}{B^2} & r_v+\frac{4d_2}{B^2} & 0 \\ 0 & 0 & d_3 \end{bmatrix},$$

$$\mathbf{K}^{st} = \begin{bmatrix} k_1+\frac{2k_2}{B^2} & -\frac{2k_2}{B^2} & \frac{m_p x_g g}{B} \\ -\frac{2k_2}{B^2} & k_1+\frac{2k_2}{B^2} & -\frac{m_p x_g g}{B} \\ \frac{m_p x_g g}{B} & -\frac{m_p x_g g}{B} & 2k_3 - g m_p z_g \end{bmatrix}. \tag{25}$$

4. Parameter identification

To develop a control scheme for the system, the parameters of the derived model must be determined. The geometric properties, including actuator placement and metrology platform dimensions, are derived from CAD data and dimensional measurements on the setup, and these parameters are fixed for subsequent parameter identification. The remaining system parameters, such as masses, inertia matrices, stiffness, and damping parameters, are estimated based on CAD data and then exactly identified on the experimental setup by a grey-box model identification process. This is done by fitting simulated time-domain trajectories of the model to reference measurements from the experimental setup. For the identification the *greyest* command from *Matlab* is used, which employs a subspace Gauss–Newton least-squares algorithm [22]. Various input steps on $\mathbf{f}_q^e$ are applied to the system to excite the platform dynamics with the dynamic coupling between the generalized coordinates $\mathbf{q}$, as shown in Fig. 6. The small arrows in the plot indicate, which generalized force is applied respectively. The reduced linear model in the stiction regime is used for the parameter identification and the input forces are chosen, to keep the forces on the linear carts below their stiction force. This way, friction effects are excluded from the parameter identification process.

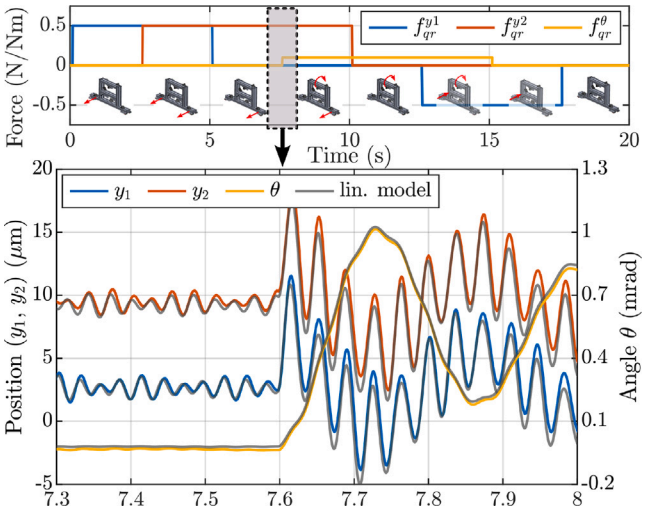

Fig. 6. (Top) Input force steps applied to the metrology platform in the stiction regime. (Bottom) Representative section of measured platform positions (colored) and simulated trajectories of the reduced linear model (gray) with the fitted model parameters. (For interpretation of the references to color in this figure legend, the reader is referred to the web version of this article.)

In the bottom plot of Fig. 6 a representative section of the platform position measurement is shown, together with the simulated trajectories of the model based on the fitted system parameters. The response of the reduced linear model matches the measurement very well, which justifies the assumptions made during model simplification in the previous section. The validation of the model for the sliding regime will be demonstrated in the next sections.

5. Control design

Based on the derived linear system models, in this section a decoupled motion control scheme is developed to control the 3 DoF of the metrology platform.

5.1. System decoupling

The coupled 2nd-order equations of motion (23), (25) are decoupled by using a modal analysis approach [23]. This procedure involves finding the modal matrix $\mathbf{U}$, which transforms the coupled differential equations of motion into a new set of decoupled equations in new principal coordinates $\boldsymbol{\nu} = \mathbf{U}^{-1}\mathbf{q}_r$. For undamped systems the solution of the generalized eigenvalue problem

$$\lambda\mathbf{M}\mathbf{u} = \mathbf{K}\mathbf{u}, \quad \mathbf{U} = \begin{bmatrix} \mathbf{u}_1 & \mathbf{u}_2 & \ldots & \mathbf{u}_n \end{bmatrix} \tag{26}$$

directly leads to the modal matrix $\mathbf{U}$, which diagonalizes the $\mathbf{M}$ and $\mathbf{K}$ matrix of the mechanical system [23]. For damped systems, the condition $\mathbf{D}\mathbf{M}^{-1}\mathbf{K} = \mathbf{K}\mathbf{M}^{1}\mathbf{D}$ has to be fulfilled, to simultaneously decouple the $\mathbf{D}$ matrix [24]. Although this is not the case for the derived linear models, the approach is still viable, since the developed feedback controller can cope with the remaining coupling via the damping matrix.

After solving (26) for both linear models and normalizing $\mathbf{U}$, such that $\mathbf{U}^T\mathbf{M}_r\mathbf{U} = \mathbf{I}$, the equations of motion in the new coordinates $\boldsymbol{\nu}$ are written as

$$\underbrace{\mathbf{U}^T\mathbf{M}_r\mathbf{U}}_{\mathbf{M}_{dec}=\mathbf{I}}\ddot{\boldsymbol{\nu}} + \underbrace{\mathbf{U}^T\mathbf{D}\mathbf{U}}_{\mathbf{D}'}\dot{\boldsymbol{\nu}} + \underbrace{\mathbf{U}^T\mathbf{K}\mathbf{U}}_{\mathbf{K}_{dec}}\boldsymbol{\nu} = \underbrace{\mathbf{U}^T\mathbf{W}_r\mathbf{f}_r^e}_{\mathbf{f}_{dec}}. \tag{27}$$

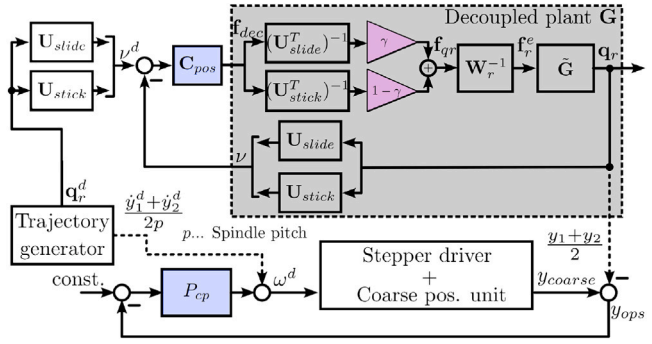

Fig. 7. Dual-stage control concept with decoupling transformation. A cross-fading gain γ is used to switch between the stiction and sliding model.

The result are two 3-dimensional mechanical system models for each friction regime (sliding, stiction) in the new coordinates $\boldsymbol{\nu}$, with the input force vector $\mathbf{f}_{dec}$, the diagonal mass and stiffness matrices ($\mathbf{M}_{dec}$, $\mathbf{K}_{dec}$), and the damping matrix $\mathbf{D}'$.

5.2. Dual-stage control concept

Given the derived system (27), 3 SISO position controller are designed in the frequency domain for the coordinates $\boldsymbol{\nu}$. A block-diagram of the implemented control scheme is shown in Fig. 7. The transfer matrix $\tilde{\mathbf{G}}$ represents the plant with the LA forces $\mathbf{f}_r^e$ as input and the generalized coordinates $\mathbf{q}_r$ as output. By applying the mapping between generalized forces and LA forces $\mathbf{W}_r^{-1}$ and the decoupling transformation with the modal matrix $\mathbf{U}_j$ with $j \in \{sl, st\}$, the gray box in the figure represents the decoupled plant $\mathbf{G}$ from (27).

In the transition between static (stiction regime) and moving platform (sliding regime) and vice-versa, the modal matrix $\mathbf{U}$ from Fig. 7 has to be switched from the stiction model to the sliding model, to maintain the decoupling between the controlled coordinates. As shown in Fig. 7, the transition is done by combining a weighted sum of both decoupling matrices with a smooth function $\gamma(t) \in [0, 1]$ [25]. The transition function from stiction to sliding is defined as minimum-jerk trajectory

$$\gamma(t) = 6\left(\frac{t}{T}\right)^5 - 15\left(\frac{t}{T}\right)^4 + 10\left(\frac{t}{T}\right)^3 , \tag{28}$$

for $t \in [0, T]$. For the transition from sliding to stiction, the roles of γ and $1-\gamma$ are exchanged.

The decoupled plant (gray box) is the base for the design of 3 SISO PID position controllers. In the implementation on the experimental prototype system, the LA forces $\mathbf{f}_r^e$ are converted to actuator currents with the known actuator force constant k_a according to

$$\mathbf{i}_{vca} = \frac{1}{k_a}\mathbf{f}_{vca} , \tag{29}$$

and are controlled by underlying PI current-controllers. As the current control loops are designed for a bandwidth well above the targeted motion control bandwidth (10 kHz), they are treated as unity-gain for the position control design.

In order to keep the LAs in their actuation range, the coarse positioning unit has to follow the metrology platform accordingly [15]. As the used stepper motor driver takes the angular velocity ω of the motor as input, a low-bandwidth proportional position controller P_{cp} is used to keep the y-distance between pusher and platform constant (see Fig. 2). As the movement of the platform is usually known a-priori, it is additionally applied to the stepper motor driver in a feed-forward manner

$$\omega_{ff} = \frac{\dot{y}_1^d + \dot{y}_2^d}{2p} , \tag{30}$$

with p being the mechanical spindle pitch.

5.3. Position control design

The goal of the position controller $\mathbf{C}_{pos}$ is to follow with the metrology platform a desired motion trajectory, as given by the trajectory generator in Fig. 7. Since the desired trajectory is given in the generalized coordinates $\mathbf{q}_r^d$, they are transformed to the previously introduced modal coordinates $\boldsymbol{\nu}$ with the modal matrix $\mathbf{U}$. Three PID-position controllers are designed with the control output force $\mathbf{f}_{dec}$, which is then translated to the actual forces of the LAs ($\mathbf{f}_r^e$). To verify the decoupling from Section 5.1 and to enable the control design in the frequency domain, the transfer matrix of the decoupled plant (gray box in Fig. 7) is measured for both derived linear system models. Therefore the platform is stabilized with low-bandwidth position controllers and the measurement is performed in a closed-loop manner [26]. To enable measurements in the sliding regime, the platform is moved with a constant velocity of 10 mm/s by the controllers during each measurement run.

The measured bode plot of the MIMO transfer matrix for each friction regime is shown in Fig. 8, in which the colored lines represent the new introduced coordinates $\boldsymbol{\nu} = \mathbf{U}^{-1}\mathbf{q}_r$ together with the associated motion shape. As expected, each coordinate shows classical second-order spring-mass-damper behavior until structural modes of the system emerge beyond 150 Hz. One exception is G_{33} in the sliding regime, due to the fact, that the stiffness k_1 disappears in moving direction and only the viscous damping of the linear cart friction acts against the movement (yellow motion shape in the right plot of Fig. 8).

On top of the measurement the theoretical transfer functions with the fitted model parameters from the previous section are plotted (dotted lines), which match the measurement very well in both regimes, validating the modeling assumptions from Section 3.3. The mismatch between model and measurement of G_{11} in the sliding regime results from the fact, that the additional weight added by the linear carts (m_c) is neglected in the linear model, which leads to a slightly larger total mass and increased moment of inertia I_{zz} around the z-axis (refer to Fig. 4) of the platform during sliding. Consequently the mass line is shifted down for lower frequencies until the additional weight gets decoupled from the motion at approximately 60 Hz (red box in Fig. 8), which also leads to the shift of the resonance frequency. This simplification is acceptable, since the position control bandwidth of the feedback controller is beyond this decoupling frequency. The gray curves in the plot represent the cross-coupling between the coordinates, which is introduced by the damping matrices of (25) and deviations of the linear model from the real system. Up to approximately 200 Hz the cross-coupling magnitude is below the main-diagonal transfer functions, justifying the implementation of independent SISO controllers for each DoF.

Since the mass-line of each main-diagonal transfer function is aligned due to the normalization $\mathbf{U}^T\mathbf{M}_r\mathbf{U} = \mathbf{I}$, for each degree of freedom the same control parameters can be used. The position controllers are implemented as PID-controller with the structure

$$C_{pid}(s) = k_p + \frac{k_{I,p}}{s} + \frac{k_d s}{1 + sT_t} , \tag{31}$$

and tuned to the open-loop cross-over frequency f_c [14]. To suppress unmodeled structural modes at higher frequencies, 14 notch-filters

$$C_{n,i}(s) = \frac{s^2 + 2D_i\xi_i\omega_{n,i}s + \omega_{n,i}^2}{s^2 + 2\xi_i\omega_{n,i}s + \omega_{n,i}^2} , \tag{32}$$

with the notch-frequency $\omega_{n,i}$, damping coefficient D_i, and notch width parameter ξ_i are tailored to the measured responses for each regime [14]. The position controller $\mathbf{C}_{pos}$ is then given by

$$\begin{aligned} \mathbf{C}_{pos}(s) &= \mathrm{diag}\left(C_{pos}, C_{pos}, C_{pos}\right) , \\ C_{pos}(s) &= C_{pid}(s) \cdot \prod_i C_{n,i}(s) . \end{aligned} \tag{33}$$

As the difference position between pusher and metrology platform is less critical, as long as the LAs are in their operation range, a simple

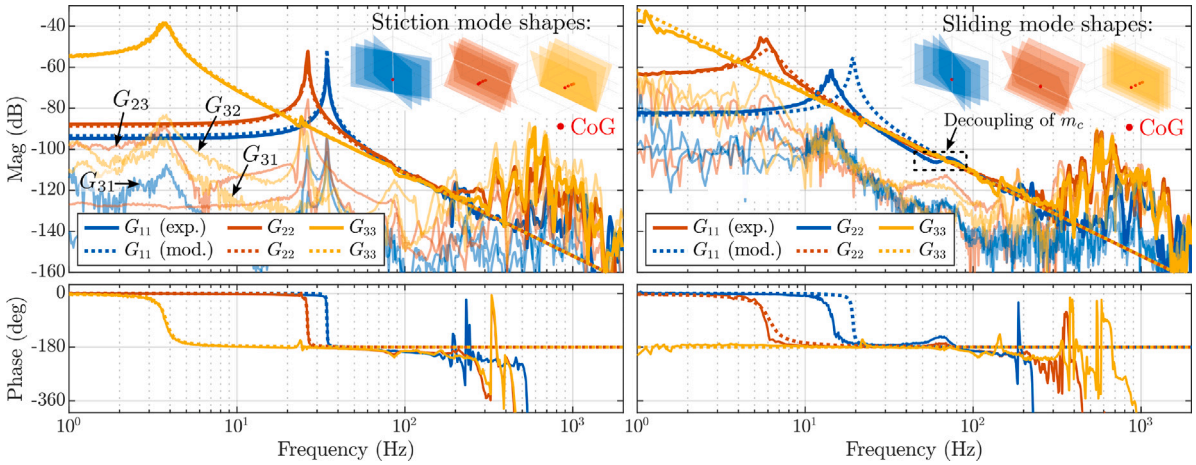

Fig. 8. Measured transfer functions of decoupled system (solid lines) and linear system models with the fitted system parameters (dotted lines) for the stiction regime (left) and the sliding regime (right). Additionally the modal shapes for each friction regime are shown, which are associated with the respective decoupled principal coordinates $\boldsymbol{\nu} = \mathbf{U}^{-1}\mathbf{q}_r$. The transparent lines represent the coupling from one coordinate to another with the respective color. (For interpretation of the references to color in this figure legend, the reader is referred to the web version of this article.)

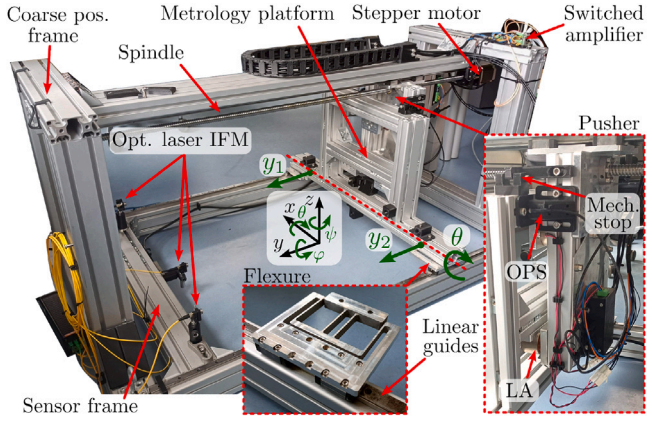

Fig. 9. Experimental setup of the 3-DoF positioning system. The metrology platform is guided on the machine frame by linear guides and the designed crab-leg flexure mounts. It is driven by the LAs on the pusher and the spindle-drive.

Table 1
System and control parameters.

System parameters					
a	172 mm	b	167 mm	c	119 mm
d	12 mm	B	562 mm	B_{ifm}	570 mm
H_{ifm}	140 mm	x_g	−3.8 mm	y_g	−3.4 mm
z_g	148 mm	m_p	7.9 kg	m_c	0.22 kg
k_1	47 200 N m^{-1}	k_2	1700 N m rad^{-1}	k_3	92 N m rad^{-1}
d_1	−4.7 N s m^{-1}	d_2	0.28 N m s rad^{-1}	d_3	1.12 N m s rad^{-1}
J_{xx}	0.13 kg m^2	J_{yy}	0.41 kg m^2	J_{zz}	0.215 kg m^2
p	10 mm	k_a	12.7 N A^{-1}		
Position controller C_{pid}, P_{cp}					
k_p	5.6×10^4	k_I	1.76×10^6	k_d	4.45×10^2
T_t	4.97×10^{-4}	P_{cp}	1.35×10^3		
Notch-filter coefficients ($C_{n,i}(s)$)					
$\frac{\omega_{n,i}}{2\pi}$	245, 325, 454, 550, 600, 681, 713, 750 796, 930, 1089, 1245, 1815, 2375				
D_i	0.006, 0.01, 0.1, 0.056, 0.018, 0.032, 0.032, 0.316 0.1, 0.1, 0.018, 0.032, 0.178, 0.003				
ξ_i	0.25, 0.13, 0.05, 0.15, 0.2, 0.1, 0.1, 0.08 0.08, 0.25, 0.15, 0.15, 0.1, 0.8				

proportional controller P_{cp} is used to complement the feed-forward of the platform-velocity as depicted in Fig. 7. The proportional gain is tuned for a desired open-loop crossover frequency $f_{c,cp}$.

6. Experimental validation

6.1. Experimental setup

To validate the designed system and control scheme, the positioning system from Fig. 2 is built as shown in Fig. 9. The spindle is driven by a stepper motor (103-H5210-4200, RTA, IT) with stepper motor driver (DM542T, StepperOnline, US). The three LAs (VCAR0087-0062-00A, Supt Motion, CN) mounted on the pusher and metrology platform are driven by custom made switched current amplifiers [27].

The crab-leg flexure mounts are designed for a sufficient low stiffness in the actuated DoFs to keep the actuators in their force limits, while simultaneously restricting the motion in the non-actuated DoFs to negligible small values tuned by mechanical FEM simulations. Additionally mechanical stops are added, to keep the flexures within their mechanical stress limits.

Position measurement is done via 3 optical laser interferometers (IFM) (IDS3010, AttoCube Systems AG, GER) mounted on the sensor frame and by an optical proximity sensor (OPS) (TCND5000, Vishay, US) mounted on the pusher. The sensor readout and control system is implemented on a rapid prototyping system (MicroLab-Box, dSPACE GmbH, GER). The position controller are tuned to an open-loop crossover frequency of $f_c = 80$ Hz to keep the control bandwidth below the structural modes occuring beyond 240 Hz, as can be seen in Fig. 8. In Table 1 the identified system parameters and tuned control parameters for the experimental setup are summarized. They are discretized for the implementation on the rapid prototyping system with a sampling-rate of 10 kHz.

6.2. Measurement errors related to positioning system

For the evaluation of the system, the lateral measurement uncertainty originating from the positioning system is of interest. Therefore, the measured position of the metrology platform is used to calculate the resulting error $\Delta y_m(x,t)$, as shown in Fig. 1. By using $\psi = \tan^{-1}\left(\frac{y_1 - y_2}{B}\right)$, the measurement error $y_m(x,t)$ can be expressed by

$$\Delta y_m(x,t) = \left[\frac{y_1 + y_2}{2} + h_i \tan(\theta) + x\tan(\psi)\right] - y^d\,, \tag{34}$$

with the coordinates y_1, y_2, θ and the effective standoff height of the measurement systems h_i. The maximum error along the x-axis is

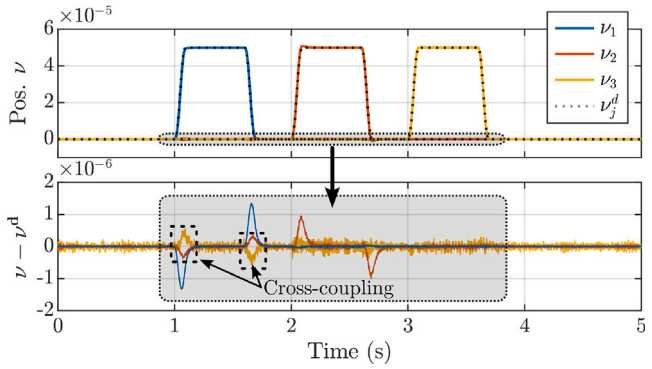

Fig. 10. Fast position changes of the decoupled coordinates $\boldsymbol{\nu}$ in the stiction regime (Platform stands still). In the bottom plot a zoomed-in section of the motion error is plotted.

calculated for a given inspection width w_i according to

$$\epsilon_m(t) = \max_x \left(\Delta y_m(x,t)\right) \text{, for } x \in \left[-\frac{w_i}{2}, \frac{w_i}{2}\right] . \tag{35}$$

This represents the worst-case measurement error in y-direction over time at any point on the inspection area. For the subsequent validation $w_i = 0.6\,\text{m}$ and $h_i = 0.55\,\text{m}$ are used, which corresponds to the working distance and field of view of two commercially available 3D surface measurement sensors (SC 2500-300, Micro-Epsilon GmbH, GER) mounted side by side (Fig. 1) [28].

6.3. Evaluation

The control performance and coordinate decoupling are first evaluated in the stiction regime by executing fast position changes in the decoupled coordinates $\boldsymbol{\nu}$, as shown in Fig. 10. Therefore the reference trajectories, indicated by dotted lines, are applied to the control system's reference input $\boldsymbol{\nu}^d$, with additional feedforward forces based on the modeled main-diagonal transfer functions from Fig. 8 added to $\mathbf{f}_{dec}$. The bottom plot presents a zoomed-in view of the motion errors, confirming a maximum error of less than 2.5 % of the position end-value throughout the entire trajectory. As expected from the measured transfer functions in Fig. 8 and the fact, that the damping matrix of (23) cannot be simultaneously decoupled by the presented modal decoupling, some residual coupling between coordinates is observed, particularly for ν_1 and ν_2. However, the implemented decentralized control scheme effectively suppresses these coupling effects, keeping the induced errors within an acceptable small range.

For the precision evaluation in the sliding regime, the platform is moved along the entire range (0...0.7 m) with varying velocities v. In Fig. 11 a motion trajectory with a constant velocity of $v = 10\,\text{mm/s}$ is shown. For the desired motion profile $y^d(t)$ a piece-wise polynomial function is used, comprised of an acceleration-phase (gray in Fig. 11) with a fixed distance of 10 mm, followed by the measurement phase with constant velocity v and a deceleration-phase (gray) for 10 mm. On the top, the motion trajectory $y^d(t)$ together with the transitioning function $\gamma(t)$ is visible, which is set for a duration of $T = 1\,\text{s}$. The transition between the stiction and sliding model is started at the start of the acceleration and deceleration phase respectively. Additionally to the positioning error, the previously defined worst-case measurement error in y-direction $\epsilon_m(t)$ is plotted. The resulting worst-case error is 7.5 µm (rms) in the measurement phase.

Additionally the worst-case deviation for the spindle-drive alone (SD) is shown in the third plot (blue curve). Therefore the spindle is driven with a constant velocity of 10 mm/s and the metrology platform is fixed at the pusher by applying a constant current of −0.8 A to all three LAs. Due to manufacturing imperfections and mounting tolerances of the linear guides the overall error is approximately 1000 µm

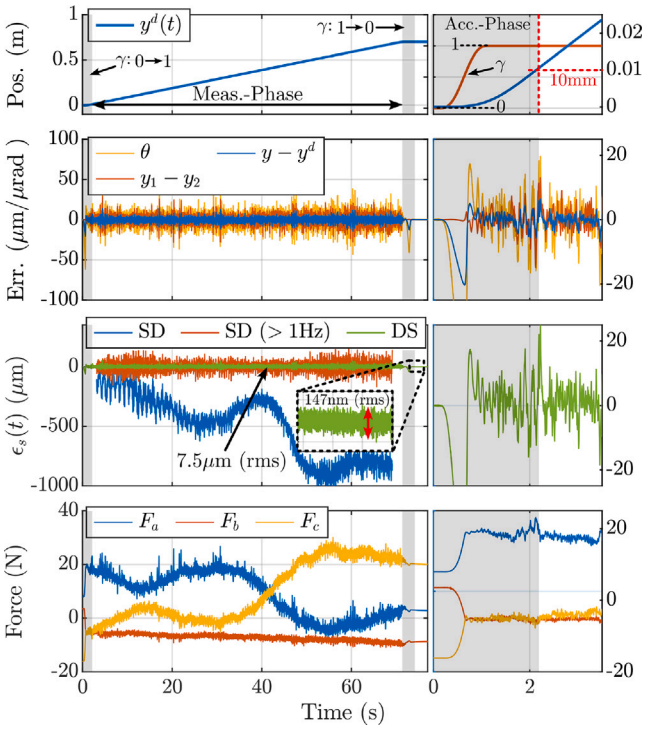

Fig. 11. Metrology platform motion errors and resulting measurement error $\epsilon_m(t)$ for 10 mm/s velocity in dual-stage (DS) and spindle-drive mode (SD). Entire range (left plots) and zoomed section (right plots). The acceleration and deceleration phase (10 mm) are shaded gray.

over the entire range. However, since this overall and slow trend is repeatable and could be reduced by adapting the driving speed, the error signal is high-pass filtered ($f_c = 0.5\,\text{Hz}$) to show the higher frequent (non-correctable) errors (red curve). With an error of 38 µm (rms) in the measurement phase, it is still over a factor of 5 worse than in DS mode.

In the bottom plot the actuator forces (F_a, F_b, F_c) in DS-mode are depicted. It is visible, that the LAs correct the slow trend due to manufacturing imperfections and mounting tolerances, to exactly align the platform with the sensor frame. The slow force trend is superimposed by the high-frequent correction forces of the LAs, which are necessary to compensate for disturbing forces acting on the platform. When the platform is in idle state, a static measurement uncertainty of 147 nm (rms) can be achieved. This extremely low error is possible, because the spindle-drive does not move in this case, and consequently no disturbing vibrations from the coarse positioning unit can be transmitted to the metrology platform via the machine frame.

Additionally to the time-domain, the error $\epsilon_m(t)$ is also analyzed in the frequency domain for varying velocities v. The power spectral density (PSD) and cumulative amplitude spectrum (CAS) over frequency for the measurement phase are shown in Fig. 12. From the figure it can be seen, that the resulting measurement errors originating from the positioning system range from 7.5 µm (rms) for 10 mm/s (Fig. 11) to 12.3 µm (rms) for 100 mm/s. The main contributors to the errors are in the lower frequency range of up to 60 Hz. Afterwards only a structural mode at 240 Hz has a visible impact at higher speeds.

Additionally, the PSD over spatial frequency is shown on the right side of Fig. 12, in which errors related to a certain moving distance of the platform become independent from the velocity v. As highlighted with the gray area in the bottom right plot, the low-frequent errors show a strong spatial periodicity at fractions of the mechanical spindle pitch of 10 mm. These errors result from disturbance forces originating from the stepper motor and the spindle-drive, which are transmitted to the metrology platform via the machine frame.

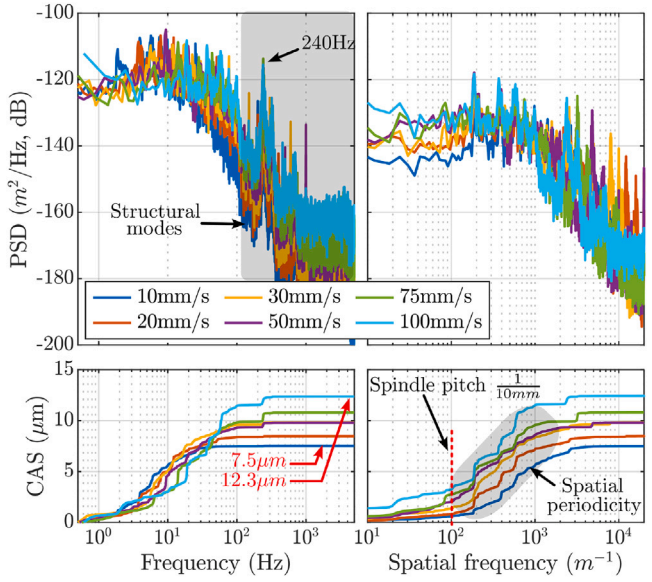

Fig. 12. Power spectral density (PSD) and cumulative amplitude spectrum (CAS) of ϵ_m for varying platform velocities over temporal frequency (left) and spatial frequency (right).

In summary, the effectiveness of the implemented control scheme for the developed dual-actuated precision positioner is successfully demonstrated on the experimental prototype. The experiments show a worst-case measurement error in moving direction of down to 7.5 µm (rms) over the entire range (0.7 m × 0.5 m) during platform motion with velocities up to 100 mm/s.

7. Conclusion

This paper presents the design of a 3-DoF precision positioning system for high-precision optical 3D inline-metrology based on a dual-stage approach, which combines a mechanical spindle-drive for large range motion with 3 Lorentz-actuators for precise motion control. Based on a general non-linear mathematical system model, two simplified linear models are derived for the stiction and sliding friction regime of the system. These models are used to perform systematic decoupling of the actuated motion DoFs by modal analysis, enabling motion control by 3 SISO PID-controllers. The presented approach is evaluated on an experimental multi DoF precision positioning system. By measuring the position errors of the metrology platform, a maximum measurement error in motion direction of down to 7.5 µm (rms) is demonstrated over a large inspection area (0.7 m × 0.5 m) during platform motion with speeds up to 100 mm/s. This is a vast improvement compared to spindle-drive alone and proves the validity of the approach for the use in high-precision inline-metrology applications. Further, a static measurement error resulting from the positioning system of 147 nm (rms) can be achieved for the given measurement configuration.

Future work will focus on further reducing the remaining errors by incorporating the strong spatial periodicity at fractions of the spindle pitch into the control design, as well as on experiments in combination with optical measurement systems mounted on the metrology platform.

CRediT authorship contribution statement

Daniel Pechgraber: Writing – original draft, Visualization, Validation, Methodology, Investigation, Formal analysis. **Ernst Csencsics:** Writing – review & editing, Supervision, Funding acquisition. **Georg Schitter:** Writing – review & editing, Supervision, Funding acquisition.

Declaration of competing interest

The authors declare the following financial interests/personal relationships which may be considered as potential competing interests: Daniel Pechgraber reports financial support was provided by Christian Doppler Research Association. If there are other authors, they declare that they have no known competing financial interests or personal relationships that could have appeared to influence the work reported in this paper.

Acknowledgments

The financial support by the Austrian Federal Ministry of Economy, Energy and Tourism, the National Foundation for Research, Technology and Development and the Christian Doppler Research Association, and Micro-Epsilon Atensor GmbH and MICRO-EPSILON-MESSTECHNIK GmbH & Co.K.G. is gratefully acknowledged.

References

[1] Imkamp D, Schmitt R, Berthold J. Blick in die Zukunft der Fertigungsmesstechnik. Tech Mess 2012;79(10):433–9.
[2] Azamfirei V, Psarommatis F, Lagrosen Y. Application of automation for in-line quality inspection, a zero-defect manufacturing approach. J Manuf Syst 2023;67:1–22.
[3] Traxler L, Ginner L, Breuss S, Blaschitz B. Experimental comparison of optical inline 3D measurement and inspection systems. IEEE Access 2021;9:53952–63.
[4] Marxer M, Bach C, Keferstein CP. Fertigungsmesstechnik. Springer; 2021.
[5] Zanuttigh P, Marin G, Mutto CD, Dominio F, Minto L, Cortelazzo GM. Time-of-flight and structured light depth cameras :Technology and applications. Springer; 2016, p. 367.
[6] Bergmann RB, Kalms M, Falldorf C. Optical in-process measurement: Concepts for precise, fast and robust optical metrology for complex measurement situations. Appl Sci 2021;11(22):10533.
[7] Li Y, Kästner M, Reithmeier E. Vibration-insensitive low coherence interferometer (LCI) for the measurement of technical surfaces. Measurement 2017;104:36–42.
[8] Wertjanz D, Csencsics E, Kern T, Schitter G. Bringing the lab to the fab: Robot-based inline measurement system for precise 3-D surface inspection in vibrational environments. IEEE Trans Ind Electron 2022;69(10):10666–73.
[9] Schlarp J, Csencsics E, Schitter G. Optical scanning of laser line sensors for 3D imaging. Appl Opt 2018;57(18):5242.
[10] Elfizy A, Bone G, Elbestawi M. Design and control of a dual-stage feed drive. Int J Mach Tools Manuf 2005;45(2):153–65.
[11] Horowitz R, Li Y, Oldham K, Kon S, Huang X. Dual-stage servo systems and vibration compensation in computer hard disk drives. Control Eng Pract 2007;15(3):291–305.
[12] Butler H. Position control in lithographic equipment [applications of control]. IEEE Control Syst 2011;31(5):28–47.
[13] Vrijsen NH, Jansen JW, Lomonova EA. Comparison of linear voice coil and reluctance actuators for high-precision applications. In: Proceedings of 14th International Power Electronics and Motion Control Conference EPE-PEMC 2010. IEEE; 2010.
[14] Schmidt RM, Schitter G, Rankers A. The design of high performance mechatronics-: High-tech functionality by multidisciplinary system integration. Ios Press; 2020.
[15] Ito S, Steininger J, Schitter G. Low-stiffness dual stage actuator for long rage positioning with nanometer resolution. Mechatronics 2015;29:46–56.
[16] Shinno H, Yoshioka H, Sawano H. A newly developed long range positioning table system with a sub-nanometer resolution. CIRP Ann 2011;60(1):403–6.
[17] Sollapur SB, Waghmare PM, Patil M, Deshmukh S. Design and experimental testing of XY flexure mechanism. J Eng Sci Technol 2021;16(2):1416–25.
[18] Ortega R, Loría A, Nicklasson PJ, Sira-Ramírez H. Euler-Lagrange systems. In: Passivity-based control of Euler-Lagrange systems. Springer London; 1998, p. 15–37.
[19] Ling M, Howell LL, Cao J, Chen G. Kinetostatic and dynamic modeling of flexure-based compliant mechanisms: A survey. Appl Mech Rev 2020;72(3).
[20] Falkenhahn V, Mahl T, Hildebrandt A, Neumann R, Sawodny O. Dynamic modeling of bellows-actuated continuum robots using the Euler–Lagrange formalism. IEEE Trans Robot 2015;31(6):1483–96.
[21] Johanastrom K, Canudas-de Wit C. Revisiting the LuGre friction model. IEEE Control Syst 2008;28(6):101–14.
[22] Yuan Y-X. Subspace methods for large scale nonlinear equations and nonlinear least squares. Optim Eng 2008;10(2):207–18.
[23] Ma F, Morzfeld M. A general methodology for decoupling damped linear systems. Procedia Eng 2011;14:2498–502.

[24] Caughey TK, O'Kelly MEJ. Classical normal modes in damped linear dynamic systems. J Appl Mech 1965;32(3):583–8.
[25] Wertjanz D, Csencsics E, Schitter G. An efficient control transition scheme between stabilization and tracking task of a MAGLEV platform enabling active vibration compensation. In: 2020 IEEE/ASME International Conference on Advanced Intelligent Mechatronics. IEEE; 2020.
[26] Evers E, Voorhoeve R, Oomen T. On frequency response function identification for advanced motion control. In: 2020 IEEE 16th International Workshop on Advanced Motion Control. IEEE; 2020.
[27] Pechgraber D, Csencsics E, Wiesböck J, Schitter G. Switched amplifier-driven nanopositioning: Integrating system modeling and control tuning. IEEE Trans Ind Electron 2024.
[28] Micro-Epsilon GmbH & CoKG. Datasheet surfacecontrol 2500 series. 2024.